INORGANIC CHEMISTRY
FRONTIERS

CHINESE CHEMICAL SOCIETY

ROYAL SOCIETY OF CHEMISTRY

RESEARCH ARTICLE

View Article Online
View Journal | View Issue

Cite this: *Inorg. Chem. Front.*, 2024, **11**, 7979

Realizing efficient broadband near-infrared emission under blue light excitation in Sb^{3+}-doped zero-dimensional organic tin(IV)-based metal halides *via* coordination structure modulation†

Bao Ke,[a] Hui Peng, *[b] Yongqi Yang,[a] Chengzhi Yang,[a] Shangfei Yao,[a] Arfan Bukhtiar, [a] Qilin Wei,*[c] Jialong Zhao[a,b] and Bingsuo Zou *[a,b]

Received 28th July 2024,
Accepted 26th September 2024

DOI: 10.1039/d4qi01904k

rsc.li/frontiers-inorganic

Realizing Sb^{3+}-activated efficient broadband near-infrared (NIR) emission under blue light excitation remains a significant challenge in lead-free metal halides. To overcome the above difficulties, a coordination structure modulation strategy was adopted, and the broadband NIR emission under blue light excitation was achieved in Sb^{3+}-doped zero-dimensional (0D) organic tin(IV) bromide. Compared to the weak visible light emission with a photoluminescence quantum yield (PLQY) of 2.4% for pure $(TBP)_2SbBr_5$ (TBP = tetrabutylphosphonium), Sb^{3+}-doped $(TBP)_2SnBr_6$ exhibits an efficient broadband NIR emission band at 705 nm with a PLQY of 33.2% upon 452 nm excitation, which stems from self-trapped exciton emission. Combined with experiments and theoretical calculations, we find that the large excited-state lattice distortion degree compared to the ground state and the narrow bandgap are dominant reasons for Sb^{3+}-doped $(TBP)_2SnBr_6$ showing efficient NIR emission under blue light excitation. Specifically, Sb^{3+}-doped $(TBP)_2SnBr_6$ also has excellent anti-water stability, existing stably in water for more than 4 hours while maintaining a high luminous efficiency. Based on the excellent stability and unique optical properties of Sb^{3+}-doped $(TBP)_2SnBr_6$, a high-performance NIR light-emitting diode (LED) was fabricated by combining Sb^{3+}-doped $(TBP)_2SnBr_6$ with a commercial blue LED chip, and its application in night vision was demonstrated.

1. Introduction

Near-infrared (NIR) light sources are highly desired due to their low thermal effect, non-destructive nature, and deep tissue penetration, and are an ongoing pursuit for a variety of high-end applications such as night vision, food quality analysis, and biomedical imaging.[1,2] In particular, broadband NIR sources in the 700–1100 nm range have received much attention because the interaction between infrared light and infrared-active molecular bonds in food and human tissues produces wide-response characteristic absorption signals in this spectral region.[3] However, traditional NIR light sources, including halogen and tungsten lamps, are unsuitable for portable applications due to their large volumes and high working temperatures. Recently, NIR phosphor conversion LEDs (pc-LEDs), which combine broadband NIR phosphors with commercial blue LED chips, have sparked widespread attention because of their compact size, tunable broadband emission, and excellent efficiency. The NIR emitter, as an important component of NIR pc-LEDs, and its photophysical properties directly determine the performance of the device.[4] Therefore, it is crucial to develop efficient broadband NIR luminescent materials with excellent stability under blue light excitation.

Currently, many broadband NIR emitters have been reported, mainly focusing on the study of metal-ion doped oxides, such as Cr^{3+}-doped $Ga_{2-x}Sc_xO_3$,[5] Eu^{2+}-doped $K_3LuSi_2O_7$,[6] and Bi^{3+}-doped $BaAl_{12}O_{19}$.[7] However, these oxide phosphors have a high lattice energy and require high-temperature (>1000 °C) calcination to obtain the target products. Obviously, high-temperature synthesis not only results in serious energy consumption but also poses a series of safety risks in the preparation process. The above shortcomings drive us to develop efficient broadband NIR luminescent materials

---

[a] *School of Physical Science and Technology, Guangxi University, Nanning 530004, China. E-mail: zoubs@gxu.edu.cn*
[b] *State Key Laboratory of Featured Metal Materials and Life-cycle Safety for Composite Structures, and School of Resources, Environment and Materials, Guangxi University, Nanning 530004, China. E-mail: penghuimaterial@163.com*
[c] *School of Chemistry and Chemical Engineering, Shandong University, Jinan 250100, China. E-mail: qlwei@sdu.edu.cn*

† Electronic supplementary information (ESI) available. CCDC 2382097 and 2382098. For ESI and crystallographic data in CIF or other electronic format see DOI: **https://doi.org/10.1039/d4qi01904k**

that can be synthesized at low temperatures. Low-dimensional lead-free metal halides have drawn much attention because of their simple preparation method, low toxicity, and adjustable optical properties. Parallelly, they generally exhibit broadband self-trapped exciton (STE) emission due to lattice distortion and strong electron–phonon coupling. Thus, this provides an opportunity for the development of a new generation of NIR luminescent materials.

Recently, some lead-free metal halides with broadband NIR emission have been developed. For instance, Wang *et al.* synthesized Sn^{2+}-doped all-inorganic 0D Cs_2ZnBr_4, which exhibits broadband NIR emission at 700 nm with a photoluminescence quantum yield (PLQY) of 40%.[8] Moreover, Yang *et al.* reported Cu(I)-based metal halides with highly efficient broadband NIR emission.[9] However, the poor stability seriously limits their application in high-performance NIR light sources. In contrast, Sb^{3+}-activated lead-free metal halides with NIR emission have attracted wide attention due to their high efficiency and remarkable stability. For example, Sb^{3+}-doped Cs_2ZnCl_4 emits a broadband NIR emission band at 745 nm under 316 nm excitation,[10] and Sb^{3+}-doped $(NH_4)_2SnCl_6$ exhibits an NIR emission band at 736 nm under 360 nm excitation.[11] Although the aforementioned Sb^{3+}-activated NIR emitters exhibit excellent optical properties, their excitation bands are limited to the ultraviolet (UV) region, which is difficult to match with commercial blue LED chips.

To address the above concerns, we report herein a new NIR emitter of Sb^{3+}-doped tin(IV)-based metal halides *via* coordination structure modulation, which can exhibit bright broadband NIR emission under blue light excitation. Compared to the Sb(III)-based metal halide of $(TBP)_2SbBr_5$ with weak red emission (PLQY ~ 2.4%), Sb^{3+}-doped $(TBP)_2SnBr_6$ exhibits a broadband NIR emission band at 705 nm with a PLQY of 33.2% under blue light excitation. Combined with experiments and theoretical calculations, we find that the large excited-state lattice distortion degree compared to the ground state and the narrow bandgap are the dominant reasons for Sb^{3+}-doped $(TBP)_2SnBr_6$ showing efficient NIR emission under blue light excitation. Finally, given the fascinating optical properties as well as the remarkable air and anti-water stability of Sb^{3+}-doped $(TBP)_2SnBr_6$, a high-performance NIR pc-LED was fabricated by combining a commercial 460 nm blue LED chip with Sb^{3+}-doped $(TBP)_2SnBr_6$ phosphors, and we further demonstrated its application in night vision. Therefore, this work provides a feasible approach for designing efficient broadband NIR light sources based on lead-free metal halides.

2. Experimental section

Materials

Tetrabutylphosphonium bromide (TBPBr, 98%), tin(IV) bromide ($SnBr_4$, 99.0%), antimony(III) bromide ($SbBr_3$, 99%), acetonitrile (99.5%), *N*,*N*-dimethylformamide (DMF, 99.9%), and ethyl ether (Et_2O, 99.5%) were purchased from Aladdin Reagent and all materials were used without any purification.

Growth of $(TBP)_2SbBr_5$ single crystals (SCs)

$(TBP)_2SbBr_5$ SCs were synthesized by the slow evaporation method. Typically, 0.3615 g of $SbBr_3$ and 0.6786 g of TBPBr were dissolved in 5 mL of acetonitrile to form a transparent solution. Afterwards, the solution was evaporated in ambient air at 40 °C for about two days, and the bulk $(TBP)_2SbBr_5$ SCs can be obtained.

Synthesis of undoped and Sb^{3+}-doped $(TBP)_2SnBr_6$ single crystals

$(TBP)_2SnBr_6$ SCs were synthesized using the antisolvent recrystallisation method. Typically, 0.4383 g of $SnBr_4$ and 0.6786 g of TBPBr were dissolved in DMF to form a transparent solution. The $(TBP)_2SnBr_6$ SCs can then be harvested by diffusing Et_2O into the precursor solution at room temperature. In order to synthesize the Sb^{3+}-doped $(TBP)_2SnBr_6$ SCs, only x mmol $SbBr_3$ was used under otherwise identical conditions.

Characterization

The crystal structures of the two compounds were determined through single-crystal X-ray diffraction (SCXRD, IPDS II-STOE). The crystallographic data of $(TBP)_2SbBr_5$ and $(TBP)_2SnBr_6$ can be obtained for free from the Cambridge Crystallographic Data Centre (CCDC) with accession numbers 2382097 and 2382098.† Powder XRD (PXRD) measurements were acquired *via* a Bruker D8 Discover X-ray diffractometer. The PL and PLE spectra, temperature-dependent PL spectra, time-resolved photoluminescence (TRPL) spectra and PLQY were recorded using a Horiba Jobin Yvon Fluorolog-4 spectrometer. The Raman and power-dependent PL spectra were obtained using a WITec alpha300R instrument with 532 and 405 nm lasers, respectively. UV-Vis absorption spectra were recorded using a Shimadzu UV3600 Plus instrument. The morphology was observed *via* a Hitachi SU8020 scanning electron microscope (SEM), and an energy-dispersive spectrometer (EDS, Oxford X-Max Aztec) was employed to determine the composition and distribution of elements. X-ray photoelectron spectroscopy (XPS) measurements were performed using a Thermo Fisher ESCALAB 250Xi. Thermal stability was measured using a Shimadzu DTG-60H instrument in a nitrogen environment with a heating rate of 15 °C min^{-1}.

Calculation methods

The Vienna *ab initio* simulation package (VASP) was used for all calculations.[12] For the exchange and correlation functionals, the Perdew–Burke–Ernzerhof (PBE) parameterization was approximated using a generalized gradient method through the use of the projector-augmented wave method.[13,14] For the wavefunction basis set, a 4 × 4 × 3 Monkhorst–Pack *k*-mesh for $(TBP)_2SbBr_5$ and 4 × 3 × 3 for $(TBP)_2SnBr_6$, and a 500 eV kinetic energy cutoff were used. For each element, ultrasoft pseudopotentials were employed. For structural relaxations, the energy convergence threshold was established at

1.0×10^{-5} eV. To calculate the lattice distortion of the excited state structure, the crystal structure of the excited state must first be obtained. The detailed process is as follows: first, the ground state structure is obtained through a standard VASP optimization and relaxation process. Then, the EIGENVAL file from the static calculation is read to examine the occupation of relevant electrons. By adding FERWE and FERDO to control the spin occupation of electrons, the excited state structure is relaxed. Finally, using eqn (1), the bond lengths of the excited state structure are analyzed to determine the degree of distortion in the excited state.

$$\Delta d = \left(\frac{1}{n}\right) \sum_{i=1}^{n} \left[\frac{d_n - d_{\text{ave}}}{d_{\text{ave}}}\right]^2 \quad (1)$$

where d_n is the distances of Sb–Br bonds, d_{ave} denotes the average Sb–Br bond length, and n is the number of Sb–Br bonds.

NIR pc-LED fabrication

The as-synthesized Sb^{3+}-doped $(TBP)_2SnBr_6$ SCs were ground into powders, then mixed in AB glue to form a uniform mixture, and finally coated onto a 460 nm LED chip. Subsequently, the performance parameters of the as-fabricated NIR pc-LED were measured using an Everfine HAAS-2000 instrument.

3. Results and discussion

Two bulk assemblies of 0D organic metal halides of $(TBP)_2SbBr_5$ and $(TBP)_2SnBr_6$ with various coordination structures were synthesized *via* a simple solution method at room temperature (RT), and their crystal structures were determined by single-crystal X-ray diffraction (SCXRD). As shown in Fig. 1a and b, the crystallographic units of the two as-synthesized compounds both contain two TBP^+ cations and a different inorganic polyhedron, that is, square-pyramidal $[SbBr_5]^{2-}$ clusters for $(TBP)_2SbBr_5$ and octahedron-shaped $[SnBr_6]^{2-}$ clusters for $(TBP)_2SnBr_6$. The isolated polyhedra are separated from each other and periodically embedded in the framework of organic cations in both compounds, thus constituting a typical 0D structure. Moreover, $(TBP)_2SbBr_5$ crystallizes in the triclinic space group $P\bar{1}$, while $(TBP)_2SnBr_6$ adopts the monoclinic space group $C2/c$. As shown in Fig. 1c, the distance of Sb–Br drops in the range of 2.52–2.78 Å in the $[SbBr_5]^{2-}$ unit of $(TBP)_2SbBr_5$, while that of Sn–Br ranges from 2.59 to 2.63 Å in the $[SnBr_6]^{2-}$ octahedron of $(TBP)_2SnBr_6$. More detailed crystallographic data of $(TBP)_2SbBr_5$ and $(TBP)_2SnBr_6$ are summarized in Tables S1–S3,† and their different crystal structure will bring different optical properties. In particular, there are large M–M (M = Sn and Sb) distances >9.6 Å in both compounds, which indicates that there is a negligible interaction between adjacent inorganic polyhedra.[15] Fig. 1d shows the PXRD measurements of $(TBP)_2SbBr_5$ and $(TBP)_2SnBr_6$, and the diffraction patterns were consistent with the simulated ones, which demonstrates the dependability of SCXRD results.

Then, a series of Sb^{3+}-doped $(TBP)_2SnBr_6$ with various doping concentrations were synthesized. The structures of Sb^{3+}-doped $(TBP)_2SnBr_6$ are given in Fig. 1b. Clearly, Sb^{3+} ions can be substituted for Sn^{4+} sites due to their similar ion radii (CN = 6, $r_{Sb^{3+}}$ = 76 pm and $r_{Sn^{4+}}$ = 69 pm) and exist in the form of the $[SbBr_6]^{3-}$ octahedron in the Sb^{3+}-doped $(TBP)_2SnBr_6$ compound. The PXRD patterns of Sb^{3+}-doped $(TBP)_2SnBr_6$ with various doping concentrations are similar to that of the pristine $(TBP)_2SnBr_6$, indicating that the doping of Sb^{3+} does not change the crystal structure of the host matrix (Fig. 1e). Table S4† shows the EDS results of Sb^{3+}-doped $(TBP)_2SnBr_6$, and it can be seen that the doping concentration of Sb^{3+} is much lower than the feed content. Fig. S1† shows the high-resolution X-ray photoelectron spectroscopy (HRXPS) spectra of Sb 3d. Compared with $(TBP)_2SbBr_5$, the characteristic peaks of Sb^{3+} $3d_{5/2}$ and Sb^{3+} $3d_{3/2}$ in Sb^{3+}-doped $(TBP)_2SnBr_6$ shift towards a lower binding energy (0.3 eV), which should be due to Sb^{3+} ions having different coordination chemical environments in the above two compounds. The weak signal-to-noise ratio of Sb^{3+} in HRXPS indicates the low Sb^{3+} content, which echoes the EDS results well. Moreover, the SEM images of these two compounds are given in Fig. 1f and S2,† and the elemental mapping shows the uniform distribution of Sn, Sb, and Br in $(TBP)_2SbBr_5$ and Sb^{3+}-doped $(TBP)_2SnBr_6$. The morphology and size of single crystals are shown in Fig. S3;† both types of single crystals exhibit a yellow color under natural light, with sizes ranging from 2 to 10 mm. They display irregular block-like structures and have good transparency.

The optical properties of the as-synthesized compounds were measured at RT. For $(TBP)_2SnBr_6$, the UV-vis absorption spectrum showed an optical absorption edge at 468 nm, and the bandgap value was determined to be 2.78 eV through the Kubelka–Munk function (Fig. S4†). Moreover, $(TBP)_2SnBr_6$ is a yellow crystal in natural light and shows very weak PL emission under photoexcitation (Fig. S3a†). The PL and PLE spectra of $(TBP)_2SnBr_6$ are given in Fig. S5.† Clearly, this compound exhibits a broadband emission band at 480 nm with a full width at half-maximum (FWHM) of 78 nm. Normally, there are three mechanisms for the single PL emission in metal halides apart from the influence of organic molecules, namely, permanent defects, free excitons, and STEs.[11] We analyzed the possibility of a respective mechanism that governs the emission in $(TBP)_2SnBr_6$ as follows: (i) the optical properties of TBPBr were also measured (Fig. S6†), which are greatly different from those of $(TBP)_2SnBr_6$, thus excluding the influence of the organic ligand on the optical properties of $(TBP)_2SnBr_6$; (ii) we measured the variation of emission with respect to the excitation power and found that the PL intensity exhibits linear dependence on the excitation power (Fig. S5a†). This rules out the permanent defect mechanism, otherwise the emission intensity should be saturated with an increase in the power density;[16] (iii) the broad FWHM and large Stokes shift in $(TBP)_2SnBr_6$ are completely inconsistent with the free exciton mechanism since free excitons usually have smaller Stokes shifts and narrower FWHMs (Fig. S5b†);[17] and (iv) the excitation wavelength-dependent PL spectra of $(TBP)_2SnBr_6$ show

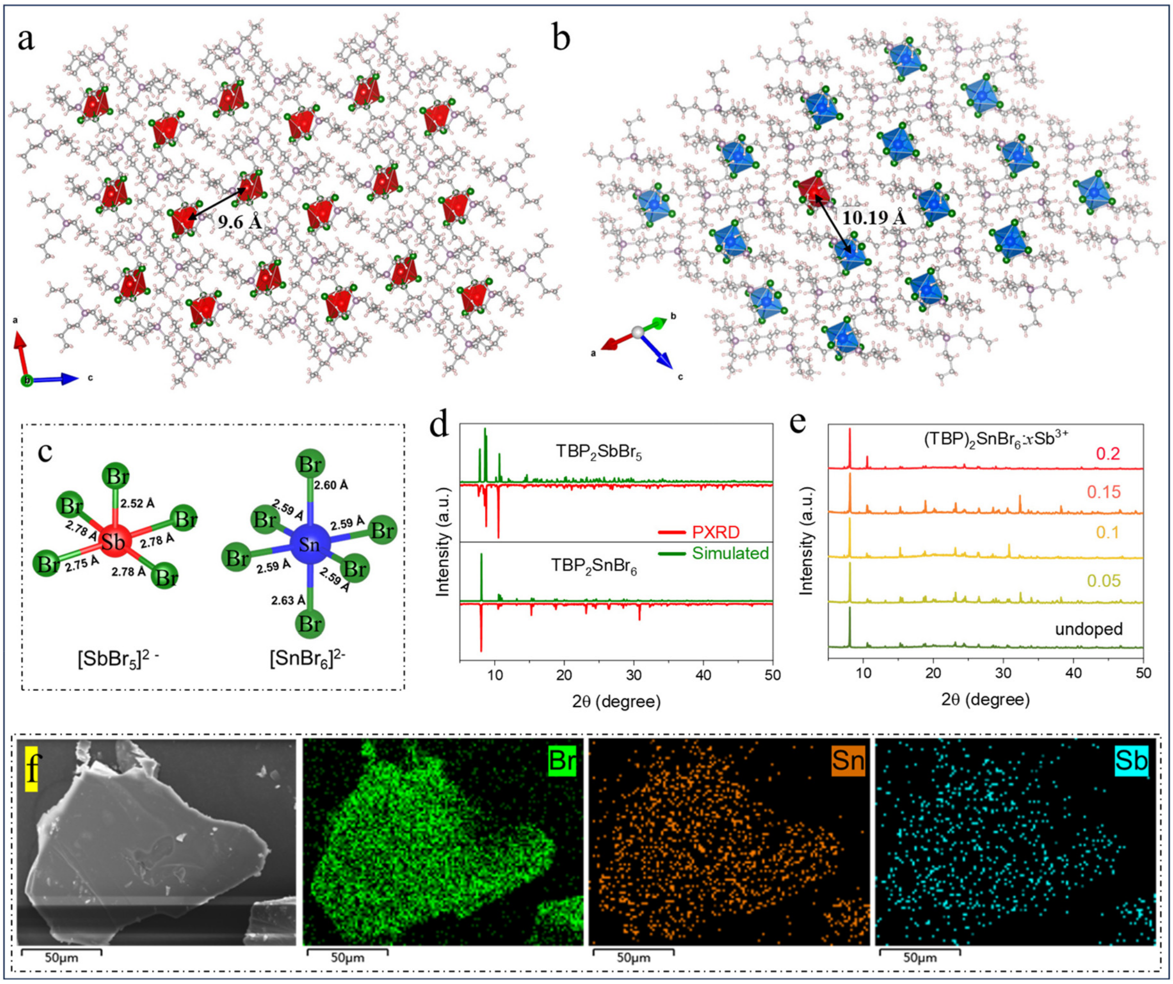

Fig. 1 Crystalline structures of (a) $(TBP)_2SbBr_5$ and (b) Sb^{3+}-doped $(TBP)_2SnBr_6$. (c) A ball-and-stick model of $[SbBr_5]^{2-}$ and $[SnBr_6]^{2-}$ clusters. (d) Experimental and calculated PXRD patterns of $(TBP)_2SbBr_5$ and $(TBP)_2SnBr_6$. (e) PXRD patterns of Sb^{3+}-doped $(TBP)_2SnBr_6$. (f) SEM and EDS elemental mapping of $0.15Sb^{3+}$-doped $(TBP)_2SnBr_6$.

an identical profile, which illustrates that the observed PL stems from the same excitation state (Fig. S5c†). The average lifetime of the emission is 17.6 ns (Fig. S5d†), which is comparable to those of recently reported organic Sn(IV) halides with STE emission.[16,18] Combining the unique photophysical properties discussed above, we can reasonably attribute the broadband emission observed in $(TBP)_2SnBr_6$ to STE emission.[19]

However, $(TBP)_2SnBr_6$ shows weak emission (PLQY < 1%), which severely restricts its further applications in photoelectric devices. Recently, Sb^{3+}-activated low-dimensional metal halides have attracted extensive attention due to their fascinating optical properties.[20–22] In order to improve the optical properties of $(TBP)_2SnBr_6$ and further understand the reasons for their efficient emission, we synthesized Sb^{3+}-doped $(TBP)_2SnBr_6$ and the pure Sb(III)-based metal halide of $(TBP)_2SbBr_5$, respectively. Then, the PL and PLE spectra of $(TBP)_2SbBr_5$ and Sb^{3+}-doped $(TBP)_2SnBr_6$ were recorded at RT, and the corresponding optical images are given in Fig. S3b and S3c.† As shown in Fig. 2a and b, both compounds have an intense excitation band within the blue light region (470 nm for $(TBP)_2SbBr_5$ and 452 nm for Sb^{3+}-doped $(TBP)_2SnBr_6$). Upon blue light excitation, $(TBP)_2SbBr_5$ shows a broad visible emission band at 660 nm, while Sb^{3+}-doped $(TBP)_2SnBr_6$ exhibits a NIR emission band at 705 nm. As a consequence, the two compounds have a large Stokes shift of 0.76 eV for $(TBP)_2SbBr_5$ and 0.98 eV for Sb^{3+}-doped $(TBP)_2SnBr_6$. Moreover, the above two compounds also exhibit long PL decay lifetimes of 0.73 and 1.22 μs, respectively (Fig. S7†). Parallelly, the UV-vis absorption spectra of $(TBP)_2SbBr_5$ and $0.15Sb^{3+}$-doped $(TBP)_2SnBr_6$ are depicted in Fig. S8 and S9.† Clearly, both compounds show strong absorption in the visible light region, which corresponds to the yellow crystal in natural light (Fig. S3b and S3c†), but they have different optical absorption edges and bandgaps: 498 nm and 2.60 eV for $(TBP)_2SbBr_5$ and 475 nm and 2.76 eV for $0.15Sb^{3+}$-doped $(TBP)_2SnBr_6$. The greatly different optical properties of $(TBP)_2SbBr_5$ and Sb^{3+}-doped $(TBP)_2SnBr_6$ should be attributed to their different crystal structures, which we will discuss in detail later.

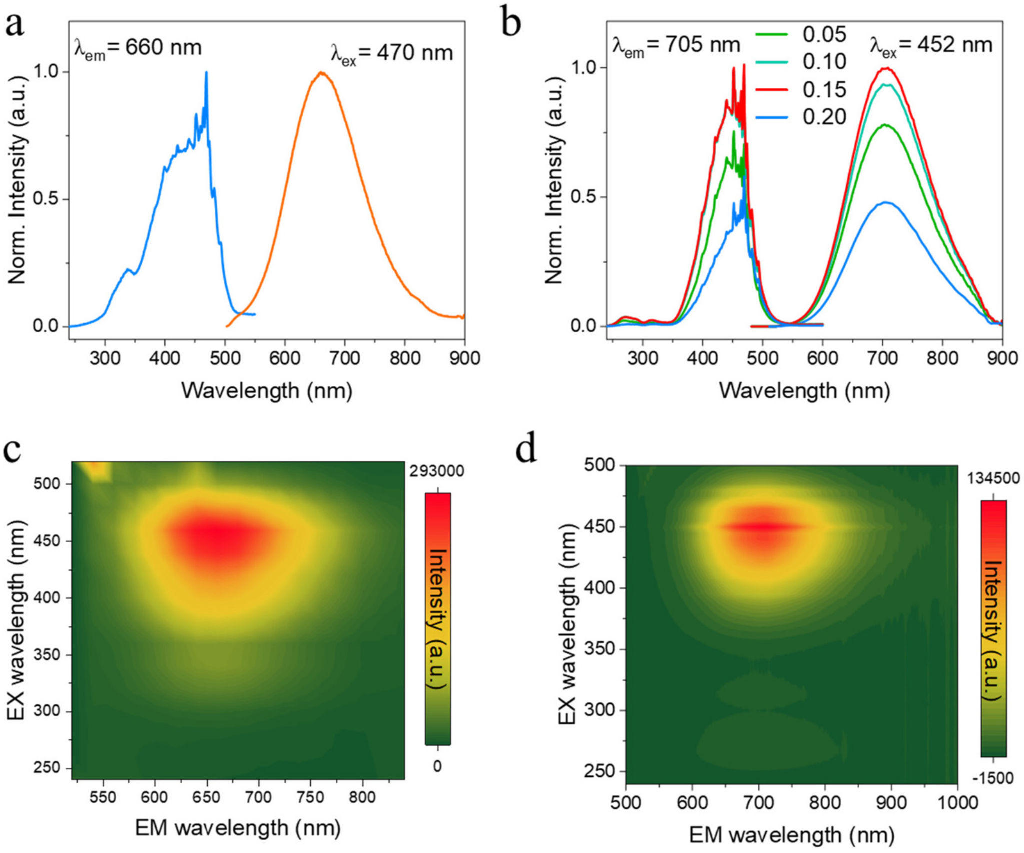

Fig. 2 (a) PL and PLE spectra of $(TBP)_2SbBr_5$ at RT. (b) PL and PLE spectra of Sb^{3+}-doped $(TBP)_2SnBr_6$ SCs with various Sb/(Sn + Sb) ratios at RT. Three-dimensional excitation–emission matrix fluorescence spectra of $(TBP)_2SbBr_5$ (c) and $0.15Sb^{3+}$-doped $(TBP)_2SnBr_6$ (d).

Subsequently, the PL spectra of Sb^{3+}-doped $(TBP)_2SnBr_6$ with various Sb^{3+} doping concentrations were recorded. As shown in Fig. 2b, the PL intensity increases first with the increase of Sb^{3+} doping concentration because more luminescence centers are generated. When the doping concentration of Sb^{3+} further increases, the emission intensity begins to decrease, which is caused by concentration quenching.[22] The strongest NIR emission in Sb^{3+}-doped $(TBP)_2SnBr_6$ can be witnessed when the feed content of Sb^{3+} is 15%, accompanied by an elevated PLQY of 33.2% (Fig. S10†). Furthermore, our Sb^{3+}-doped $(TBP)_2SnBr_6$ also has the blue light excitation characteristic, which represents the most advanced NIR emitter in lead-free metal halides (Table S5†). In contrast, the PLQY of $(TBP)_2SbBr_5$ is only 2.4%, which is difficult to meet the practical application. To further confirm the nature of broadband emission, the varying PLE and PL spectra of $(TBP)_2SbBr_5$ and Sb^{3+}-doped $(TBP)_2SnBr_6$ were recorded. As shown in Fig. 2c and d, both compounds show a broadband emission with a change in the excitation wavelength at RT, indicating that there are no other impurities or additional energy levels in the two samples. The power-dependent PL spectrum of Sb^{3+}-doped $(TBP)_2SnBr_6$ is shown in Fig. S11,† and it can be seen that the PL intensity exhibits linear dependence on the excitation power, which rules out the assumption that the emission in Sb^{3+}-doped $(TBP)_2SnBr_6$ stems from the permanent defect mechanism.[23] For $(TBP)_2SbBr_5$, besides the broadband emission band observed in Fig. 2a, there is an additional weak emission band at 510 nm (band A) with a nanosecond lifetime (3.2 ns, Fig. S12 and S13†) under 309 nm excitation at 80 K, which is different from the broadband emission band at 660 nm (band B). Although Sb^{3+}-doped $(TBP)_2SnBr_6$ exhibits a negligible change in broadband PL spectra (band B) at RT (Fig. 2d), an additional emission band at 528 nm (band A) (Fig. S14a†) with a decay lifetime of 3.18 ns can be observed under 368 nm excitation in the low-temperature PL spectra (80 K, Fig. S14b†). Moreover, the PLE spectra monitored at band A and band B exhibit different PLE spectra, which should correspond to $^1S_0 \rightarrow {}^1P_1$ (360 nm) and $^1S_0 \rightarrow {}^3P_1$ (410 nm) transition of Sb^{3+}.[21] Therefore, $(TBP)_2SbBr_5$ and Sb^{3+}-doped $(TBP)_2SnBr_6$ exhibit different optical properties, and the dual-emission bands in both compounds should stem from different excited states. Generally, for Sb^{3+} ions with a $5s^2$ electron configuration, the ground state is $^1S_0$, while the excited state is $^1P_1$, $^3P_0$, $^3P_1$, and $^3P_2$.[22] In particular, $^1S_0$–$^3P_0$ and $^1S_0$–$^3P_2$ are forbidden transitions, while $^1S_0$–$^3P_1$ and $^1S_0$–$^1P_1$ are permitted transitions because of spin–orbit coupling.[24,25] Under photoexcitation, the electrons are excited to $^3P_1$ and $^1P_1$ levels, and they will quickly be self-trapped to form two different STEs due to the large lattice distortion and strong electron–phonon coupling.[23] In our studies, the band A emission shows a short lifetime (nanosecond level) and the band B emission exhibits a long lifetime (microsecond level), which should be attributed to the two emission bands that stem from different excited states. Generally, the decay lifetime of a singlet STE is significantly shorter than that of a triplet STE, and hence the observed band A and band B emissions come from singlet and triplet STEs, respectively.[26]

Recently, numerous lead-free metal halides with efficient broadband emission have been reported, making the relationship between the crystal structure and luminescence properties a key area of research. As we know, the crystal structure of Sb^{3+} has an important influence on its optical properties.[27] In our findings, the Sb^{3+} ions have different coordination structures in $(TBP)_2SbBr_5$ and Sb^{3+}-doped $(TBP)_2SnBr_6$, which enables them to exhibit different photophysical properties. To be more specific, $(TBP)_2SbBr_5$ exhibits visible light emission, while Sb^{3+}-doped $(TBP)_2SnBr_6$ has a larger Stokes shift, resulting in efficient broadband NIR emission. Recent studies have shown that increasing the lattice distortion degree (η) of the excited state compared to the ground state is the key to yielding large Stokes shifts.[28,29] Thus, the lattice distortion parameters (Δd) of $[SbBr_5]^{2-}$ in $(TBP)_2SbBr_5$ and $[SbBr_6]^{3-}$ in Sb^{3+}-doped $(TBP)_2SnBr_6$ in the ground state (GS) and excited state (ES) were calculated using eqn (1). The calculated Δd values of $(TBP)_2SbBr_5$ and Sb^{3+}-doped $(TBP)_2SnBr_6$ are given in Tables S6 and S7.† Although the Δd value of $(TBP)_2SbBr_5$ in GS (Δd_{GS}) and ES (Δd_{ES}) is greater than that of Sb^{3+}-doped $(TBP)_2SnBr_6$, the lattice distortion degree ($\eta = (\Delta d_{ES} - \Delta d_{GS})/\Delta d_{GS}$) of $[SbBr_6]^{3-}$ is larger than that of $[SbBr_5]^{2-}$, which enables Sb^{3+}-doped $(TBP)_2SnBr_6$ to exhibit a large Stokes shift and yield a broadband NIR emission. Parallelly, a large lattice distortion can increase nonradiative losses of excitation energy, thereby quenching the PL of low-dimensional metal halides with STE emission and *vice versa*.[30,31] Therefore, Sb^{3+}-doped $(TBP)_2SnBr_6$ with appropriate lattice distortion can emit efficient emission under photoexcitation.

To further understand the broadband emission mechanism of the as-synthesized samples, the band structures and projected density of states (PDOS) of $(TBP)_2SbBr_5$, $(TBP)_2SnBr_6$, and Sb^{3+}-doped $(TBP)_2SnBr_6$ were calculated *via* density functional theory (DFT). All compounds show a direct bandgap with values of 1.15 eV for $(TBP)_2SbBr_5$ (Fig. 3a), 2.19 eV for $(TBP)_2SnBr_6$ (Fig. 3b), and 1.36 eV for Sb^{3+}-doped $(TBP)_2SnBr_6$ (Fig. 3c), which are smaller than the experimental values (Fig. S3, S8, and S9†), and this should be attributed to the fact that DFT calculations typically underestimate the bandgap value. Compared with pure $(TBP)_2SnBr_6$, when Sb^{3+} is introduced into the lattice, the bandgap decreases significantly, which corresponds to the redshift of the absorption band after Sb^{3+} doping. In addition, all compounds exhibit a negligible dispersion in the valence band maximum (VBM) and conduction band minimum (CBM), which illustrates a strong quantum confinement effect and is further consistent with its long M–M (M = Sn^{4+}, Sb^{3+}) distance in our 0D structures.[32] In particular, the calculated bandgaps of $(TBP)_2SbBr_5$ and Sb^{3+}-doped $(TBP)_2SnBr_6$ were much smaller than those of other 0D lead-free metal halides,[33–35] which makes them have strong absorption in the visible light region and yield bright emission under blue light excitation. Fig. 3d and g show the PDOS and partial charge density distribution of $(TBP)_2SbBr_5$. The VBM is composed of organic ligands, while Br p, Sb s, and Sb p states mainly dominate the CBM. Thus, a charge is transferred between the organic counterparts and inorganic clusters in $(TBP)_2SbBr_5$, which will weaken the PL intensity. In contrast to $(TBP)_2SbBr_5$, the VBM and CBM of $(TBP)_2SnBr_6$ are mostly contributed by an inorganic unit (Fig. 3e and h), that is, the VBM is mainly composed of the Br p state, while the CBM mainly consists of Br p and Sn s orbitals. After Sb^{3+} doping, there is little effect on the CBM, but a new impurity band appears in the VBM, which is contributed by Sb s and Br p characteristics (Fig. 3f and i). Moreover, the doping of Sb^{3+} will cause the downshift of Br p and Sn s states, which leads to the bandgap contraction. Although heterovalent doping introduces elements with different valence states, this does not necessarily lead to an increase in defects or a decrease in PLQY. In contrast, in some cases, appropriate heterovalent doping can improve the influence of defects by regulating the lattice structure and electronic environment of the material. For example, the incorporation of Sb^{3+} can form a stable local structure that passivates inherent defects in the material, thereby reducing non-radiative recombination and improving luminescence efficiency.[18] This has been demonstrated in practical studies, where the lone pair electrons of Sb^{3+} can significantly enhance the optical performance of Sn^{4+} systems by modulating the electronic structure.[22,36] In low-dimensional halide materials, Sb^{3+} doping is often accompanied by lattice distortion, which promotes the formation of STEs. STEs refer to electrons and holes that are confined to locally deformed regions of the material and release energy in the form of radiative recombination.[37] This mechanism not only prevents a decrease in luminescence efficiency but also helps to generate broadband emission and enhance the PLQY of the material. Therefore, Sb^{3+} ion doping can effectively regulate the electronic properties of $(TBP)_2SnBr_6$, which makes Sb^{3+}-doped $(TBP)_2SnBr_6$ exhibit fascinating optical properties compared with pure $(TBP)_2SnBr_6$.

To better understand the photophysical properties of $(TBP)_2SbBr_5$ and Sb^{3+}-doped $(TBP)_2SnBr_6$, temperature-dependent PL spectra were investigated at 80 to 300 K. As shown in Fig. 4a and b, the PL intensities of both compounds gradually increase with a decrease in temperature, which should be attributed to the suppression of nonradiative transitions at low temperatures. Then, the thermal activation energy (E_b) values for the two compounds were calculated using the Arrhenius equation (eqn (2)):

$$I(T) = \frac{I_0}{1 + A\mathrm{e}^{-E_b/k_B T}} \qquad (2)$$

where k_B is the Boltzmann constant and I_0 is the PL intensity at 0 K. The E_b values of $(TBP)_2SbBr_5$ and Sb^{3+}-doped $(TBP)_2SnBr_6$ are 295.6 and 83.2 meV (Fig. 4c), both of which are larger than the RT thermal ionization energy (≈26 meV). Consequently, the

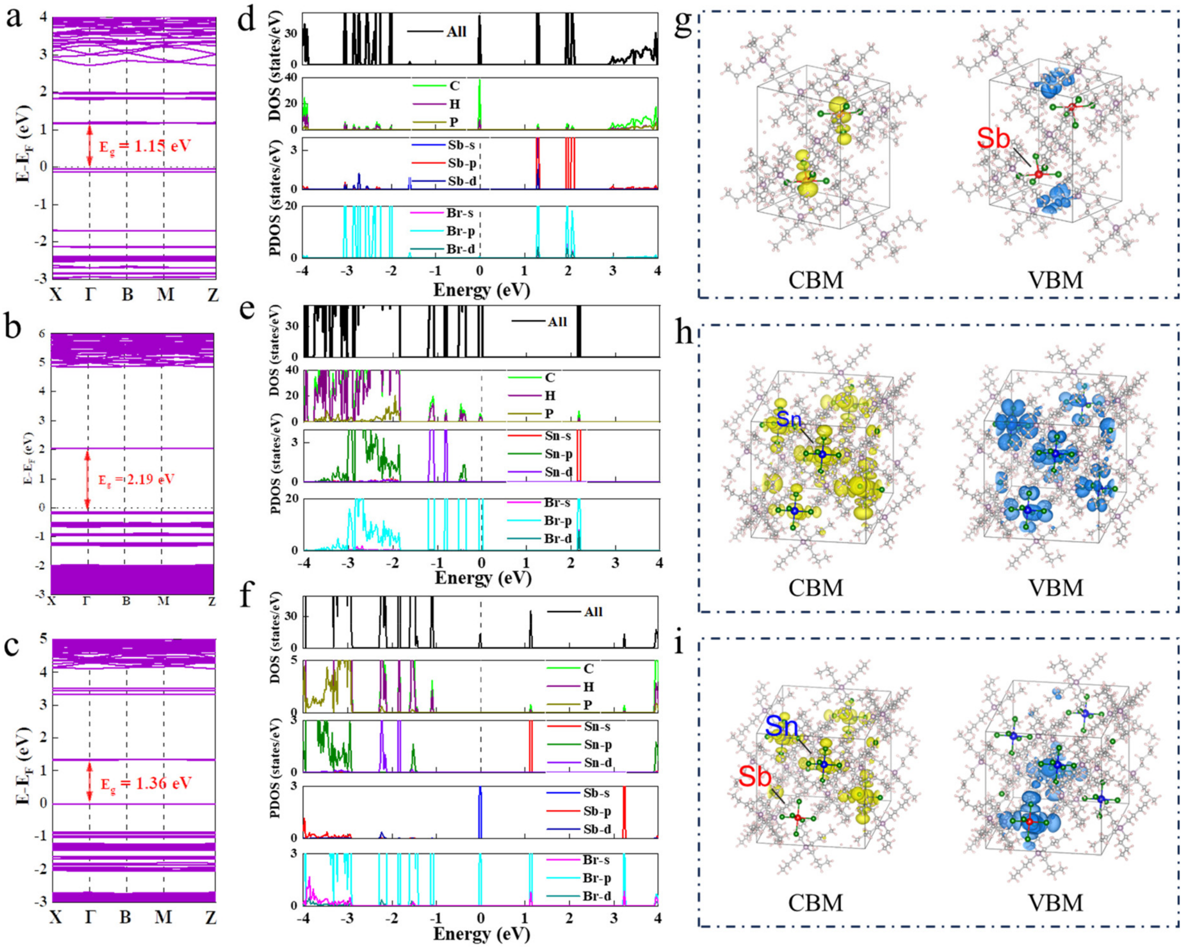

Fig. 3 Band structures and PDOS of (a and d) $(TBP)_2SbBr_5$, (b and e) $(TBP)_2SnBr_6$, and (c and f) Sb^{3+}-doped $(TBP)_2SnBr_6$. Partial charge density distribution for the CBM and VBM of (g) $(TBP)_2SbBr_5$, (h) $(TBP)_2SnBr_6$ and (i) Sb^{3+}-doped $(TBP)_2SnBr_6$.

STEs observed in Sb(III)-based and Sb^{3+}-doped compounds can exist in a stable state and overcome thermal quenching.[22]

The Huang–Rhys factor (S) is another important physical parameter that can be used to evaluate the strength of electron–phonon coupling, which can be obtained using eqn (3):

$$\mathrm{FWHM} = 2.36\sqrt{S}\hbar\omega_{\mathrm{phonon}}\sqrt{\coth\frac{\hbar\omega_{\mathrm{phonon}}}{2k_{\mathrm{B}}T}} \qquad (3)$$

where $\hbar\omega_{\mathrm{phonon}}$ represents the phonon energy. Here, the S values are 20 and 30 for $(TBP)_2SbBr_5$ and Sb^{3+}-doped $(TBP)_2SnBr_6$, respectively. Such large values of S indicate that both compounds have strong electron–phonon coupling, which guarantees the formation of STEs in these two compounds.[38] Furthermore, the difference in values of S in the above two compounds should be attributed to their different coordination configurations. Fig. 4e exhibits the temperature-dependent PLE spectra of Sb^{3+}-doped $(TBP)_2SnBr_6$. With a decrease in temperature, the PLE band exhibits a distinct blue-shift, which should be attributed to the suppression of exciton–phonon coupling as well as the reduction in thermally populated vibrations in the inorganic moiety.[18] In other words, low temperature promotes electron excitation to higher excited energy levels, resulting in the shift of the PLE band from 452 nm at RT to 410 nm at 80 K.

To gain further insight into the electron–phonon interaction, Raman spectra were obtained for pure and Sb^{3+}-doped $(TBP)_2SnBr_6$ under 532 nm laser excitation (Fig. 4f). Clearly, a series of Raman peaks are observed, which should stem from inorganic units. Among them, the Raman bands at 254, 186, 147, and 93 $\mathrm{cm^{-1}}$ perfectly meet the following formula in the octahedron: $A_{1g}^2 \approx E_g^2 + \frac{3}{2}F_{2g}^2$, where A_{1g}, F_{2g}, and E_g are the symmetric stretching, bending, and asymmetric stretching modes in $[SnBr_6]^{2-}$ units, respectively.[39] After Sb^{3+} doping, all the Raman modes shift to a lower wavenumber, which is caused by lattice expansion due to the larger ion radius of Sb^{3+} than that of Sn^{4+}.[40] In particular, Sb^{3+} doping can significantly narrow the FWHM of the Raman mode of the E_g mode and weaken the Raman intensity of the A_{1g} mode, which indicates that Sb^{3+} doping can effectively regulate the symmetry and electron–phonon coupling of the host lattice, thus bringing rich photophysical properties. Furthermore, the Raman mode at the lowest energy should be

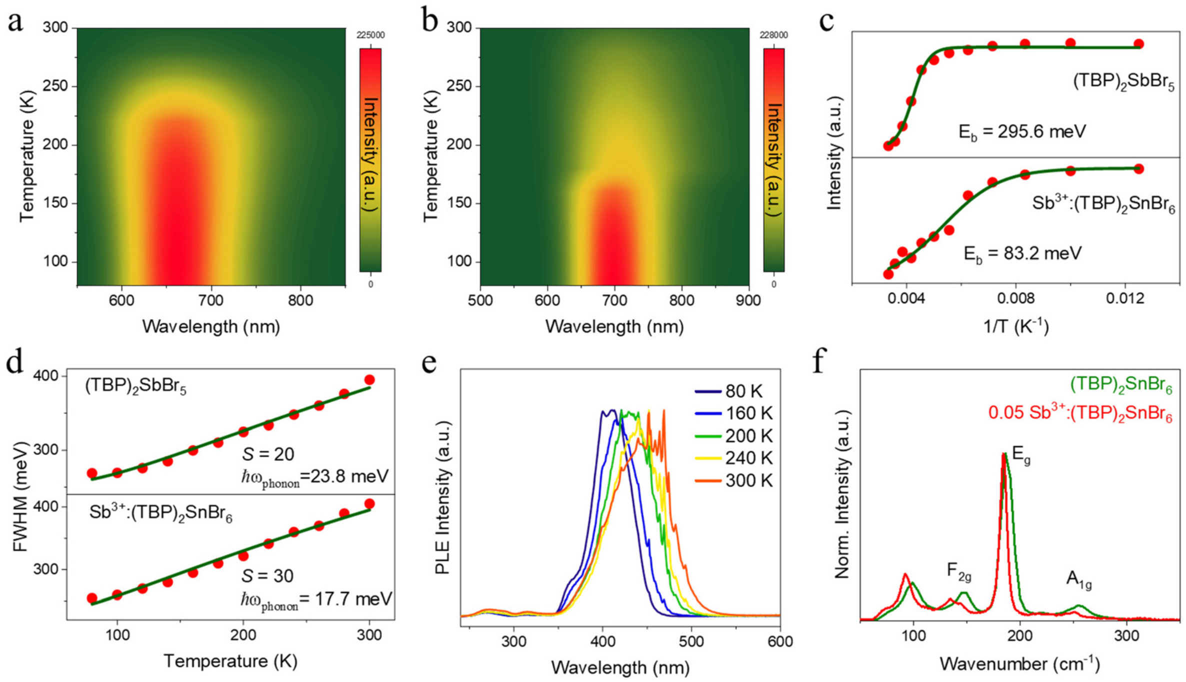

Fig. 4 Temperature-dependent PL spectra of (a) (TBP)$_2$SbBr$_5$ and (b) Sb^{3+}-doped (TBP)$_2$SnBr$_6$ within 80–300 K. (c) Integrated PL intensity of (TBP)$_2$SbBr$_5$ and Sb^{3+}-doped (TBP)$_2$SnBr$_6$ as a function of the reciprocal temperature. (d) Huang–Rhys factor of (TBP)$_2$SbBr$_5$ and Sb^{3+}-doped (TBP)$_2$SnBr$_6$. (e) PLE spectra of Sb^{3+}-doped (TBP)$_2$SnBr$_6$ with various temperatures. (f) Raman spectra of undoped and Sb^{3+}-doped (TBP)$_2$SnBr$_6$ SCs.

the strongest in strong-confined metal halides in the small polaron (STE) system.[41] However, the strongest Raman mode in this doped system is 186 cm^{-1}, which is the overtone of the 93 cm^{-1}. Their simultaneous presence means that their strong electron–phonon coupling Raman mode can be found in the just one octahedron with strong anharmonicity, resulting in an STE state within a cluster.

Based on the abovementioned results, Sb^{3+}-doped (TBP)$_2$SnBr$_6$ exhibits strong NIR emission under blue light excitation. Moreover, the optical properties of Sb^{3+}-doped (TBP)$_2$SnBr$_6$ are greatly different from those of (TBP)$_2$SnBr$_6$ and (TBP)$_2$SbBr$_5$. Combined with the crystal structure and DFT calculations, the NIR emission in Sb^{3+}-doped (TBP)$_2$SnBr$_6$ should stem from [SbBr$_6$]$^{3-}$ clusters. To identify the source of the luminescence, the Huang–Rhys factor of (TBP)$_2$SbBr$_5$ was calculated to be 30, which illustrates a strong electron–phonon interaction in this compound. Then, we recorded the power-dependent PL spectra of Sb^{3+}-doped (TBP)$_2$SnBr$_6$, and the PL intensity exhibits a linear dependence on the excitation power, which rules out the assumption that the emission in Sb^{3+}-doped (TBP)$_2$SnBr$_6$ stems from the permanent defect mechanism. Moreover, Sb^{3+}-doped (TBP)$_2$SnBr$_6$ also exhibits a large lattice distortion, broad FWHM (152 nm), large Stokes shift (0.98 eV), and long decay lifetime (1.22 μs), and thus we can confirm that the broadband NIR emission in Sb^{3+}-doped (TBP)$_2$SnBr$_6$ stems from STEs, and the photophysical mechanism is given in Fig. S16.† Under photoexcitation (*e.g.*, 452 nm), the electrons in [SbBr$_6$]$^{3-}$ clusters are excited from the ground state to the excited state. Subsequently, the excited electrons undergo quick intersystem crossing from the excited state to the triplet STE state, thus yielding a broad NIR emission peaking at 705 nm. In particular, compared with (TBP)$_2$SbBr$_5$ with visible light emission, Sb^{3+}-doped (TBP)$_2$SnBr$_6$ exhibits a larger excited state lattice distortion degree compared to the ground state, and thus this compound exhibits NIR emission under blue light excitation.

Given the excellent NIR emission characteristics of Sb^{3+}-doped (TBP)$_2$SnBr$_6$, we then investigated the stability. When Sb^{3+}-doped (TBP)$_2$SnBr$_6$ was stored in an atmospheric environment for 3 months, the PXRD patterns (Fig. S17a†) and the emission spectra show a similar outline to the pristine one. In the meantime, the PL intensity remains basically unchanged (Fig. S17b†). The thermogravimetric analysis revealed that the decomposition temperature of Sb^{3+}-doped (TBP)$_2$SnBr$_6$ is 333 °C (Fig. S17c†). Surprisingly, Sb^{3+}-doped (TBP)$_2$SnBr$_6$ also exhibits remarkable anti-water stability. As shown in Fig. 5a, Sb^{3+}-doped (TBP)$_2$SnBr$_6$ SCs can still maintain their original shape and have a high NIR emission intensity when soaked in water for 4 h. Moreover, the PL spectrum of the sample after water treatment shows a similar profile to the fresh sample (Fig. 5b), and the PLQY only dropped from 33.2 to 28.9% after soaking in water for 4 h (Fig. S18†). The PXRD patterns of Sb^{3+}-doped (TBP)$_2$SnBr$_6$ after water treatment show an identical profile to that of the fresh sample, indicating that this compound did not undergo structural degradation after soaking in water (Fig. 5c). Hence, the above results illustrate that Sb^{3+}-doped (TBP)$_2$SnBr$_6$ has excellent anti-water stability and further show that this compound emits bright NIR emission

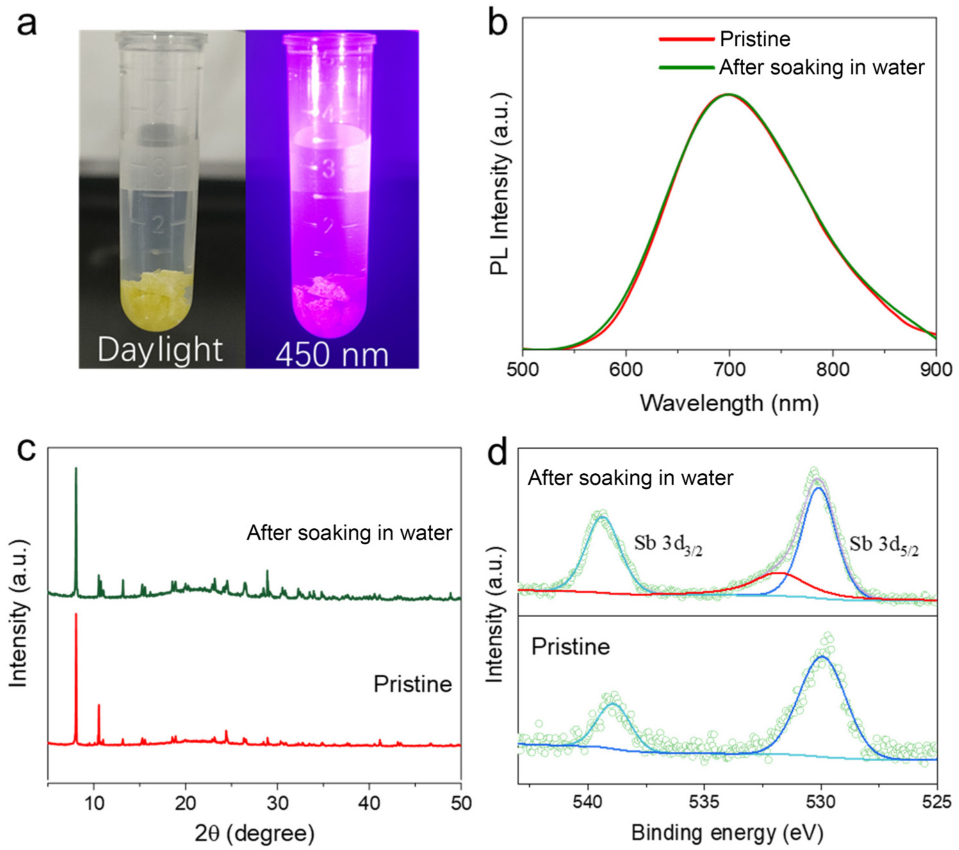

Fig. 5 (a) Digital photos of Sb^{3+}-doped $(TBP)_2SnBr_6$ under daylight (left) and 450 nm blue light (right) in water. PL stability (b), PXRD (c), and Sb 3d HRXPS results (d) of Sb^{3+}-doped $(TBP)_2SnBr_6$ after immersion in water for 4 h.

even when immersed in water. To explore the intrinsic mechanism of Sb^{3+}-doped $(TBP)_2SnBr_6$ with excellent water stability, the HRXPS spectra were recorded (Fig. 5d). Compared with the fresh sample, the sample after water treatment has an additional satellite peak at 531.9 eV, which can be assigned to the O 1s. Therefore, we believe that after this compound has been treated with water, an amorphous tin layer will form on the surface, further protecting it from degradation.[42] In the meantime, the absorption spectra exhibit a blue shift compared with the pristine sample, indicating that the formation of the oxide layer makes the optical bandgap larger (Fig. S19†). Therefore, when Sb^{3+}-doped $(TBP)_2SnBr_6$ is treated with water, an amorphous tin oxide layer can be formed on its surface to protect it from further degradation, which is the dominant reason for its excellent anti-water stability.

Finally, a high-performance NIR pc-LED was prepared by combining an Sb^{3+}-doped $(TBP)_2SnBr_6$ NIR phosphor with a blue LED chip (460 nm). Fig. 6a shows the electroluminescence (EL) spectra of the as-fabricated device, which shows a similar profile to the PL spectra. Moreover, the emission intensity of the NIR pc-LED increases gradually with an increase of driving currents (Fig. 6b), and the output power and photoelectric conversion efficiency of the device at different driving currents are given in Fig. 6c. The NIR output power increases gradually as the driving current increases, while the photoelectric conversion efficiency shows the opposite trend. The output power reaches a maximum of 9 mW at a current of 60 mA, at which point the photoelectric conversion efficiency drops to 5.4% due to the reduced efficiency of commercial LED chips.[10] In particular, the device performance parameters of the Sb^{3+}-doped $(TBP)_2SnBr_6$ based NIR pc-LED are much higher than those of the recently reported Sb^{3+}-doped Cs_2ZnCl_4 based NIR pc-LED under the same driving current,[10] which should be attributed to the fact that Sb^{3+}-doped $(TBP)_2SnBr_6$ can be excited by a blue LED chip. In further experiments, we demonstrated the application of the Sb^{3+}-doped $(TBP)_2SnBr_6$ based NIR pc-LED in night vision. In Fig. 6d, the image of a sunflower can be captured using a visible camera under sunlight, but nothing can be observed when the sunlight is turned off. In particular, the black-and-white image of a sunflower is captured using an NIR camera when the NIR pc-LED is turned on (Fig. 6f). Moreover, the operational stability of the NIR pc-LED device was measured, and the emission intensity remained high (Fig. S20†). These results demonstrate the great potential application of Sb^{3+}-doped $(TBP)_2SnBr_6$ in night vision due to the efficient NIR emission and blue-light excitation characteristics.

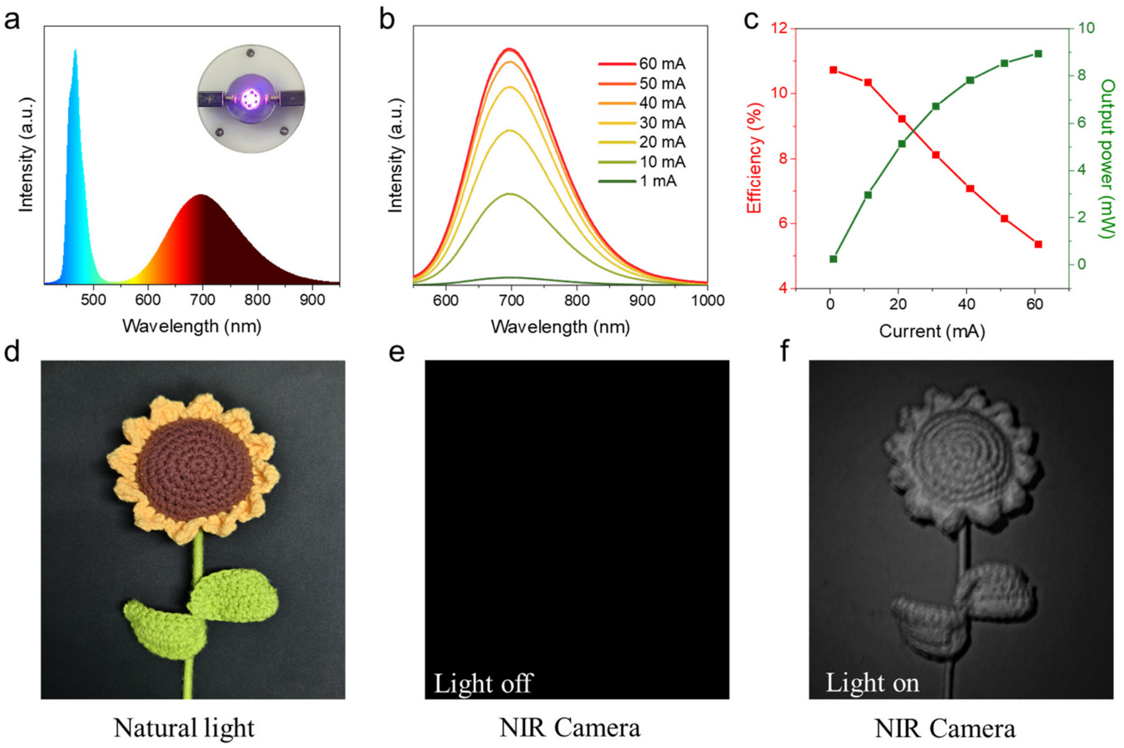

Fig. 6 (a) The EL spectra of the NIR pc-LED. (b) NIR EL spectra of the NIR pc-LED at various driving currents. (c) NIR output power and the photoelectric conversion efficiency of the device as a function of the driving current. (d–f) Physical drawing captured using visible and NIR cameras under natural and NIR light.

4. Conclusions

In summary, we report a new NIR emitter of Sb^{3+}-doped 0D $(TBP)_2SnBr_6$ *via* coordination structure modulation. Compared with pure $(TBP)_2SbBr_5$ with $[SbBr_5]^{2-}$ clusters, the coordination structure of Sb^{3+} ions in Sb^{3+}-doped $(TBP)_2SnBr_6$ can be effectively regulated to the $[SbBr_6]^{3-}$ octahedron. Combined with steady state/transient PL spectra and DFT calculations, it was found that $[SbBr_6]^{3-}$ has a larger excited state lattice distortion compared to the ground state, which will cause a large Stokes shift in Sb^{3+}-doped $(TBP)_2SnBr_6$. Moreover, Sb^{3+}-doped $(TBP)_2SnBr_6$ exhibits a narrow bandgap and multi-level non-radiative relaxation. Thus, we can obtain the efficient broadband NIR emission under blue light excitation with a PLQY of 33.2%. The study of photophysical properties illustrates that the observed broadband NIR emission in Sb^{3+}-doped $(TBP)_2SnBr_6$ stems from STE emission due to the strong electron–phonon coupling. Specifically, Sb^{3+}-doped $(TBP)_2SnBr_6$ also exhibits remarkable air and anti-water stability, and we also demonstrated the application of Sb^{3+}-doped $(TBP)_2SnBr_6$ in a high-performance NIR pc-LED. Consequently, this work not only presents a realistic proposal for designing low-dimensional lead-free metal halides with efficient broadband NIR emission under blue light excitation but also helps in understanding the relationship between the crystal structure and photophysical properties.

Data availability

The data supporting this article have been included as part of the ESI.†

Conflicts of interest

The authors declare no conflict of interest.

Acknowledgements

This work was supported by the Guangxi NSF project (no. 2020GXNSFDA238004), the "Guangxi Bagui Scholars" fund, the Guangxi Science and Technology Major Project (AA23073018), and the Scientific and Technological Bases and Talents of Guangxi (Guike AD21238027 and AD23026119) for financial support. The calculation was supported by the high-performance computing platform of Guangxi University.

References

1 Y. Wang, P. Dang, L. Qiu, G. Zhang, D. Liu, Y. Wei, H. Lian, G. Li, Z. Cheng and J. Lin, Multimode Luminescence Tailoring and Improvement of $Cs_2NaHoCl_6$ Cryolite

Crystals via Sb^{3+}/Yb^{3+} Alloying for Versatile Photoelectric Applications, *Angew. Chem., Int. Ed.*, 2023, **62**(45), e202311699.

2 W. Gan, L. Cao, S. Gu, H. Lian, Z. Xia and J. Wang, Broad-Band Sensitization in Cr^{3+}–Er^{3+} Co-Doped $Cs_2AgInCl_6$ Double Perovskites with 1.5 μm Near-Infrared Emission, *Chem. Mater.*, 2023, **35**(14), 5291–5299.

3 S. Saikia, A. Ghosh and A. Nag, Broad Dual Emission by Codoping Cr^{3+} (d-d) and Bi^{3+} (s-p) in $Cs_2Ag_{0.6}Na_{0.4}InCl_6$ Double Perovskite, *Angew. Chem., Int. Ed.*, 2023, **62**(33), e202307689.

4 Z. Wu, X. Han, Y. Zhou, K. Xing, S. Cao, L. Chen, R. Zeng, J. Zhao and B. Zou, Efficient Broadband Near-Infrared Luminescence of Cr^{3+} Doped Fluoride K_2NaInF_6 and Its NIR-LED Application Toward Veins Imaging, *Chem. Eng. J.*, 2022, **427**, 131740.

5 M.-H. Fang, K.-C. Chen, N. Majewska, T. Leśniewski, S. Mahlik, G. Leniec, S. M. Kaczmarek, C.-W. Yang, K.-M. Lu, H.-S. Sheu and R.-S. Liu, Hidden Structural Evolution and Bond Valence Control in Near-Infrared Phosphors for Light-Emitting Diodes, *ACS Energy Lett.*, 2021, **6**(1), 109–114.

6 J. Qiao, G. Zhou, Y. Zhou, Q. Zhang and Z. Xia, Divalent Europium-Doped Near-Infrared-Emitting Phosphor for Light-Emitting Diodes, *Nat. Commun.*, 2019, **10**(1), 5267.

7 Y. Wei, L. Cao, L. Lv, G. Li, J. Hao, J. Gao, C. Su, C. C. Lin, H. S. Jang, P. Dang and J. Lin, Highly Efficient Blue Emission and Superior Thermal Stability of $BaAl_{12}O_{19}:Eu^{2+}$ Phosphors Based on Highly Symmetric Crystal Structure, *Chem. Mater.*, 2018, **30**(7), 2389–2399.

8 G. Zhang, D. Wang, J. Ren, X. Zhou and Y. Wang, Highly Efficient Broadband Near-Infrared Emission from Sn^{2+} Alloyed Lead-Free Cesium Zinc Halides, *Laser Photonics Rev.*, 2023, **17**(10), 2300158.

9 X. Yang, S. M. H. Qaid, B. Wang, W. Cai, Q. Qian and Z. Zang, Broadband Near-Infrared Emission from 0D Hybrid Copper Halides, *Inorg. Chem.*, 2023, **62**(45), 18591–18598.

10 B. Su, M. Li, E. Song and Z. Xia, Sb^{3+} –Doping in Cesium Zinc Halides Single Crystals Enabling High–Efficiency Near–Infrared Emission, *Adv. Funct. Mater.*, 2021, **31**(40), 2105316.

11 H. Lin, Q. Wei, B. Ke, W. Lin, H. Zhao and B. Zou, Excitation-Wavelength-Dependent Emission Behavior in $(NH_4)_2SnCl_6$ via Sb^{3+} Dopant, *J. Phys. Chem. Lett.*, 2023, **14**(6), 1460–1469.

12 J. P. Perdew and M. Levy, Physical Content of the Exact Kohn-Sham Orbital Energies: Band Gaps and Derivative Discontinuities, *Phys. Rev. Lett.*, 1983, **51**, 1884–1887.

13 G. Kresse and J. Furthmüller, Efficient iterative schemes for ab initio total-energy calculations using a plane-wave basis set, *Phys. Rev. B: Condens. Matter Mater. Phys.*, 1996, **54**(16), 11169–11186.

14 P. E. Blöchl, Projector augmented-wave method, *Phys. Rev. B: Condens. Matter Mater. Phys.*, 1994, **50**(24), 17953–17979.

15 C. Sun, Z. Deng, Z. Li, Z. Chen, X. Zhang, J. Chen, H. Lu, P. Canepa, R. Chen and L. Mao, Achieving Near-Unity Photoluminescence Quantum Yields in Organic-Inorganic Hybrid Antimony(III) Chlorides with the $[SbCl_5]$ Geometry, *Angew. Chem., Int. Ed.*, 2023, **62**(10), e202216720.

16 G. Song, M. Li, Y. Yang, F. Liang, Q. Huang, X. Liu, P. Gong, Z. Xia and Z. Lin, Lead-Free Tin(IV)-Based Organic–Inorganic Metal Halide Hybrids with Excellent Stability and Blue-Broadband Emission, *J. Phys. Chem. Lett.*, 2020, **11**(5), 1808–1813.

17 P. Klement, N. Dehnhardt, C. Dong, F. Dobener, S. Bayliff, J. Winkler, D. M. Hofmann, P. J. Klar, S. Schumacher, S. Chatterjee and J. Heine, Atomically Thin Sheets of Lead–Free 1D Hybrid Perovskites Feature Tunable White–Light Emission from Self–Trapped Excitons, *Adv. Mater.*, 2021, **33**(23), 2100518.

18 L. Zhou, L. Zhang, H. Li, W. Shen, M. Li and R. He, Defect Passivation in Air-Stable Tin(IV)-Halide Single Crystal for Emissive Self-Trapped Excitons, *Adv. Funct. Mater.*, 2021, **31**(51), 2108561.

19 X. Liu, K. Li, W. Shao, W. Shen, M. Li, L. Zhou and R. He, Revealing the Structure–Luminescence Relationship in Robust Sn(IV)-Based Metal Halides by Sb^{3+} Doping, *Inorg. Chem.*, 2024, **63**(11), 5158–5166.

20 X. He, Q. Wei, H. Peng, Y. Li, X. Wang, B. Ke, J. Zhao and B. Zou, Large-Scale Room-Temperature Synthesis of the First Sb^{3+}-Doped Organic Ge(IV)-Based Metal Halides with Efficient Yellow Emission for Solid-State Lighting and Latent Fingerprint Detection, *Small Struct.*, 2024, **5**(5), 2300472.

21 Y. Jing, Y. Liu, M. Li and Z. Xia, Photoluminescence of Singlet/Triplet Self–Trapped Excitons in Sb^{3+} –Based Metal Halides, *Adv. Opt. Mater.*, 2021, **9**(8), 2002213.

22 B. Ke, H. Peng, Q. Wei, C. Yang, X. Li, W. Huang, Z. Du, J. Zhao and B. Zou, Achieving Highly Efficient Orange Emission in Tin(IV)–Based Metal Halides with Outstanding Anti–Water Stability Through Antimony Doping and Reasonable Structural Modulation, *Adv. Opt. Mater.*, 2024, **12**(4), 2301665.

23 J. Luo, X. Wang, S. Li, J. Liu, Y. Guo, G. Niu, L. Yao, Y. Fu, L. Gao, Q. Dong, C. Zhao, M. Leng, F. Ma, W. Liang, L. Wang, S. Jin, J. Han, L. Zhang, J. Etheridge, J. Wang, Y. Yan, E. H. Sargent and J. Tang, Efficient and Stable Emission of Warm-White Light from Lead-Free Halide Double Perovskites, *Nature*, 2018, **563**(7732), 541–545.

24 Y.-C. Peng, S.-H. Zhou, J.-C. Jin, T.-H. Zhuang, L.-K. Gong, H.-W. Lin, Z.-P. Wang, K.-Z. Du and X.-Y. Huang, $[PPh_3H]_2[SbCl_5]$: A Zero-Dimensional Hybrid Metal Halide with a Supramolecular Framework and Stable Dual-Band Emission, *J. Phys. Chem. C*, 2022, **126**(40), 17381–17389.

25 J. Wu, X. Li, X. Lian, B. Su, J. Pang, M.-D. Li, Z. Xia, J. Z. Zhang, B. Luo and X.-C. Huang, Ultrafast Study of Exciton Transfer in Sb(III)-Doped Two-Dimensional $[NH_3(CH_2)_4NH_3]CdBr_4$ Perovskite, *ACS Nano*, 2021, **15**(9), 15354–15361.

26 H. Peng, Y. Tian, Z. Yu, X. Wang, B. Ke, Y. Zhao, T. Dong, J. Wang and B. Zou, $(C_{16}H_{28}N)_2SbCl_5$: A New Lead-Free

Zero-Dimensional Metal-Halide Hybrid with Bright Orange Emission, *Sci. China Mater.*, 2022, **65**(6), 1594–1600.

27 J.-Q. Zhao, M.-F. Han, X.-J. Zhao, Y.-Y. Ma, C.-Q. Jing, H.-M. Pan, D.-Y. Li, C.-Y. Yue and X.-W. Lei, Structural Dimensionality Modulation toward Enhanced Photoluminescence Efficiencies of Hybrid Lead-Free Antimony Halides, *Adv. Opt. Mater.*, 2021, **9**(19), 2100556.

28 B. Su, G. Song, M. S. Molokeev, Z. Lin and Z. Xia, Synthesis, Crystal Structure and Green Luminescence in Zero-Dimensional Tin Halide $(C_8H_{14}N_2)_2SnBr_6$, *Inorg. Chem.*, 2020, **59**(14), 9962–9968.

29 S. Yu, H. Peng, Q. Wei, T. Li, W. Huang, X. He, Z. Du, J. Zhao and B. Zou, Realizing Efficient Broadband Near-Infrared Emission and Multimode Photoluminescence Switching via Coordination Structure Modulation in Sb^{3+}-Doped 0D Organic Metal Chlorides, *Mater. Horiz.*, 2024, **11**, 2230–2241.

30 X. Han, P. Cheng, R. Shi, Y. Zheng, S. Qi, J. Xu and X.-H. Bu, Linear Optical Afterglow and Nonlinear Optical Harmonic Generation from Chiral Tin(IV) Halides: The Role of Lattice Distortions, *Mater. Horiz.*, 2023, **10**(3), 1005–1011.

31 X. He, H. Peng, Q. Wei, Z. Zhou, G. Zhang, Z. Du, J. Zhao and B. Zou, Realizing Efficient Emission and Triple-Mode Photoluminescence Switching in Air-Stable Tin(IV)-Based Metal Halides via Antimony Doping and Rational Structural Modulation, *Aggregate*, 2024, **5**(1), e407.

32 D.-Y. Li, Y.-B. Shang, Q. Liu, H.-W. Zhang, X.-Y. Zhang, C.-Y. Yue and X.-W. Lei, 0D Hybrid Indium Halide as a Highly Efficient X-Ray Scintillation and Ultra-Sensitive Fluorescent Probe, *Mater. Horiz.*, 2023, **10**(11), 5004–5015.

33 V. Morad, Y. Shynkarenko, S. Yakunin, A. Brumberg, R. D. Schaller and M. V. Kovalenko, Disphenoidal Zero-Dimensional Lead, Tin, and Germanium Halides: Highly Emissive Singlet and Triplet Self-Trapped Excitons and X-Ray Scintillation, *J. Am. Chem. Soc.*, 2019, **141**(25), 9764–9768.

34 M. Yin, B. Li, Z. Yi, Y. Zhang, Z. Xia and Y. Xu, Crystal-Glass Phase Transition Enabling Reversible Fluorescence Switching in Zero-Dimensional Antimony Halides, *Chem. Commun.*, 2023, **59**(76), 11361–11364.

35 Q. Wei, T. Chang, R. Zeng, S. Cao, J. Zhao, X. Han, L. Wang and B. Zou, Self-Trapped Exciton Emission in a Zero-Dimensional $(TMA)_2SbCl_5 \cdot DMF$ Single Crystal and Molecular Dynamics Simulation of Structural Stability, *J. Phys. Chem. Lett.*, 2021, **12**(30), 7091–7099.

36 J. Jin, Y. Wang, K. Han and Z. Xia, Rigid Phase Formation and Sb^{3+} Doping of Tin(IV) Halide Hybrids toward Photoluminescence Enhancement and Tuning for Anti–Counterfeiting and Information Encryption, *Angew. Chem., Int. Ed.*, 2024, e202408653.

37 M. D. Smith and H. I. Karunadasa, White-Light Emission from Layered Halide Perovskites, *Acc. Chem. Res.*, 2018, **51**(3), 619–627.

38 L. Zhou, J.-F. Liao, Y. Qin, X.-D. Wang, J.-H. Wei, M. Li, D.-B. Kuang and R. He, Activation of Self-Trapped Emission in Stable Bismuth-Halide Perovskite by Suppressing Strong Exciton–Phonon Coupling, *Adv. Funct. Mater.*, 2021, **31**(31), 2102654.

39 H. Siddique, Z. Xu, X. Li, S. Saeed, W. Liang, X. Wang, C. Gao, R. Dai, Z. Wang and Z. Zhang, Anomalous Octahedron Distortion of Bi-Alloyed $Cs_2AgInCl_6$ Crystal via XRD, Raman, Huang–Rhys Factor, and Photoluminescence, *J. Phys. Chem. Lett.*, 2020, **11**(22), 9572–9578.

40 H. Peng, T. Huang, B. Zou, Y. Tian, X. Wang, Y. Guo, T. Dong, Z. Yu, C. Ding, F. Yang and J. Wang, Organic-Inorganic Hybrid Manganese Bromine Single Crystal with Dual-Band Photoluminescence from Polaronic and Bipolaronic Excitons, *Nano Energy*, 2021, **87**, 106166.

41 D. Emin, Optical Properties of Large and Small Polarons and Bipolarons, *Phys. Rev. B: Condens. Matter Mater. Phys.*, 1993, **48**(18), 13691–13702.

42 Z. Tan, Y. Chu, J. Chen, J. Li, G. Ji, G. Niu, L. Gao, Z. Xiao and J. Tang, Lead–Free Perovskite Variant Solid Solutions $Cs_2Sn_{1-x}Te_xCl_6$: Bright Luminescence and High Anti–Water Stability, *Adv. Mater.*, 2020, **32**(32), 2002443.